1 **Full Title: Mechanically Resolved Imaging of Bacteria using Expansion Microscopy**

2

3 **Short Title: Mechanically Resolved Bacterial Imaging**

4

5 **Authors:** Youngbin Lim[1], Margarita Khariton[1], Keara M. Lane[1], Anthony L. Shiver[1], Katharine

6 M. Ng[1], Samuel R. Bray[1], Jian Qin[2], Kerwyn Casey Huang[1,3,4], Bo Wang[1,5,*]

7

8 **Affiliations:**

9 [1]Department of Bioengineering, Stanford University, Stanford, CA 94305, USA

10 [2]Department of Chemical Engineering, Stanford University, Stanford, CA 94305, USA

11 [3]Department of Microbiology and Immunology, Stanford University School of Medicine,

12 Stanford, CA 94305 USA

13 [4]Chan Zuckerberg Biohub, San Francisco, CA 94158, USA

14 [5]Department of Developmental Biology, Stanford University School of Medicine, Stanford, CA

15 94305, USA

16

17 *Correspondence should be addressed to B.W. (wangbo@stanford.edu).

**Abstract**

Imaging dense and diverse microbial communities has broad applications in basic microbiology and medicine, but remains a grand challenge due to the fact that many species adopt similar morphologies. While prior studies have relied on techniques involving spectral labeling, we have developed an expansion microscopy method (μExM) in which cells are physically expanded prior imaging and their expansion patterns depend on the structural and mechanical properties of their cell walls, which vary across species and conditions. We use this phenomenon as a quantitative and sensitive phenotypic imaging contrast orthogonal to spectral separation in order to resolve bacterial cells of different species or in distinct physiological states. Focusing on host-microbe interactions that are difficult to quantify through fluorescence alone, we demonstrate the ability of μExM to distinguish species within a dense community through *in vivo* imaging of a model gut microbiota, and to sensitively detect cell-envelope damage caused by antibiotics or previously unrecognized cell-to-cell phenotypic heterogeneity among pathogenic bacteria as they infect macrophages.

## Introduction

Imaging of heterogeneous bacterial populations has broad applications in understanding the complex microbiota that exist on and within our bodies, as well as complex host-microbial interfaces, yet remains a significant challenge due to the lack of suitable tools for distinguishing species and identifying altered physiological states [1–3]. Analyses to date have mostly relied on spectral separation using fluorescence in situ hybridization (FISH) with probes designed to target 16S RNA sequences specific to certain taxa [4], or genetically engineered microbes that express distinct fluorescent proteins [5]. However, these methods are generally insensitive to physiological changes in bacterial cells that are often modulated by host environments and believed to be critical for the growth and spatial organizations of microbes [6,7].

The bacterial cell wall is a macromolecule responsible for shape determination in virtually all bacteria. Although little is known about the molecular architecture of the cell wall in most non-model organisms, its dimensions can vary widely, with the wall typically thick (tens of nanometers [8,9]) in Gram-positive species and thin (~2-4 nm) in Gram-negative species [10], and their rigidity can vary across ~10-100 MPa for Young's modulus [11,12]. The cell wall also has various biochemical compositions [13] and exhibit distinct spatial patterns of cross-linking density [14], molecular organization [15,16], thickness [8,9], and stiffness [11,12], all of which depend on species and cell physiology. Thus, cell wall mechanics can potentially provide a contrast that is orthogonal to spectral separation in distinguishing species and even cellular physiological states. However, while cell-wall structure and mechanics have been measured by electron microscopy and atomic force microcopy [8,10,17], these methods are low-throughput and incompatible with dense bacterial populations or *in vivo* applications.

55

56    To address this challenge, we develop a new method that extends the application of expansion

57    microscopy (ExM) to bacteria, particularly in the contexts of multispecies communities and

58    infection. ExM is a recently developed optical imaging method that was designed to provide

59    superior resolution to traditional fluorescence imaging, but its applications to bacteria have so far

60    been limited [18]. ExM relies on simple chemistry in which biomolecules are anchored to

61    hydrogel networks, and then membranes are permeabilized by detergents while proteins are

62    digested by proteases to allow physical expansion. The expanded sample can be imaged through

63    conventional optical microscopy and digitally compressed to gain resolution. While prior studies

64    have focused on achieving uniform expansion of samples [19–21], we posited that differences in

65    the expandability of the cell wall could provide imaging contrast that reflects its molecular

66    structural and mechanical properties.

67

68    In this study, we show that the peptidoglycan cell wall requires additional treatments to break

69    down for expansion. We demonstrate, with both *in vitro* and *in vivo* applications, that the

70    contrast in cell-wall expandability is sufficient to resolve different bacterial species within dense

71    communities. In addition, this method is sensitive enough to detect cell-wall damages due to

72    antibiotics or host defensive responses that are otherwise difficult to capture using traditional

73    imaging methods. We anticipate this method to enable future research in three major areas: (1)

74    super-resolution imaging of bacterial subcellular components [22] without the need for

75    expensive optics or special fluorophores; (2) high-content imaging that integrates both spectral

76    and mechanical contrasts to dissect complex microbial communities; and (3) *in vivo* phenotyping

77    of cell-wall mechanics and integrity [4,23].

4

78    **Results**

79

80    **Expansion provides quantitative imaging contrast to distinguish bacterial species**

81    To test whether the cell wall indeed restricts expansion in ExM, we imaged a mixture of two

82    common symbiotic bacteria isolated from the gut of the fruit fly *Drosophila melanogaster*,

83    *Acetobacter tropicalis* (GFP-labeled) and *Lactobacillus plantarum* (mCherry-labeled) [24], using

84    a standard ExM protocol (**Fig. 1A**, top) [25]. We quantified the expansion ratio of individual

85    cells based on cell width, because width can be measured precisely regardless of cellular

86    orientation in three dimensions. We found that *A. tropicalis* and *L. plantarum* cells only

87    expanded ~1.9- and ~1.2-fold, respectively (**Fig. 1B**, top), both of which were smaller than the 4-

88    fold expansion expected from previous characterizations of ExM [19,25].

89

90    We then digested the wall using lysozyme from chicken egg white or mutanolysin from

91    *Streptomyces globisporus,* after permeabilizing the cell membrane with methanol. Both enzymes

92    are muramidases that cleave 1,4-beta-linkages between N-acetylmuramic acid and N-acetyl-D-

93    glucosamine residues in the cell wall but differ in mechanism of action and activity [26].

94    Overnight lysozyme treatment enhanced the contrast in expansion ratios between species (**Fig.**

95    **1A,B**, bottom left): *A. tropicalis* cells were fully expanded ~4-fold, whereas *L. plantarum* cells

96    were largely unaffected. By contrast, mutanolysin treatment led to 4-fold expansion of both

97    species (**Fig. 1A,B**, bottom right). The uniform expansion enabled us to resolve individual cells

98    in densely packed mixed colonies of the two species while preserving their relative positions

99    (**Fig. 1C–E**).

100

5

101    Next, we tested whether these findings could be extended to other commensal species from the

102    human gut. We applied the method to seven species, including *Escherichia coli*, *Salmonella*

103    *enterica*, *Acidaminococcus intestini*, *Bacteroides finegoldii*, *Parabacteroides distasonis*,

104    *Bifidobacterium breve*, and *Clostridium innocuum*. These species were chosen to include both

105    Gram-positives and Gram-negatives. For all species, the expansion ratios were approximately 4-

106    fold after mutanolysin treatment, whereas the ratios after lysozyme treatment were generally

107    larger for all Gram-negative species than for Gram-positives (**Table 1** and **S1 Fig.**), but varied

108    widely, in particular among Gram-negatives (**Fig. 1B**, bottom left). Together, these results show

109    that the extent of breakdown of the cell wall determines the expansion of bacterial cells, and the

110    expansion ratio provides quantitative and fine resolution in distinguishing species beyond the

111    tradition classification of Gram-negatives and Gram-positives. Henceforth, we refer to this

112    method involving lysozyme or mutanolysin digestion as μExM, expansion microscopy of

113    microbes.

114

115    Our findings suggest that μExM both improves imaging resolution, as shown in previous studies

116    [19–21,25], and provides an additional imaging contrast associated with cell-wall mechanical

117    properties that is orthogonal to spectral separation commonly used in fluorescence microscopy.

118    We posited that in some cases, the contrast in expansion should be sufficient to distinguish

119    between microbial species with differing cell-wall properties (**Fig. 1F**). Moreover, this contrast

120    can be amplified by partial wall digestion using lysozyme. For example, the post-lysozyme

121    expansion ratio distributions of four species, *L. plantarum*, *Escherichia coli*, *A. tropicalis*, and

122    *Acidaminococcus intestini*, were clearly distinct, despite the variation across cells of the same

123    genotype (**Fig. 1B**, bottom left). To directly test our hypothesis, we mixed populations of *L.*

124  *plantarum* and *E. coli* cells, as they are of similar pre-expansion size and morphology and thus

125  difficult to distinguish (**Fig. 1G**). Following lysozyme treatment and expansion, the two species

126  could be easily separated by post-expansion size (**Fig. 1H**).

127

128  **Expansion detects cell-wall damage induced by antibiotics with high sensitivity**

129  Given that expansion is dependent upon cell-wall properties, we reasoned that μExM should also

130  reveal different expansion phenotypes in cells grown under conditions that generate cell-wall

131  damage. Vancomycin is an antibiotic that binds to peptidoglycan precursors and prevents their

132  crosslinking to the existing cell wall. While *E. coli* and most Gram-negative bacteria are

133  typically resistant to vancomycin, the *imp4213* allele in the *lptD* gene, which disrupts synthesis

134  of the lipopolysaccharide component of the outer membrane, leads to a permeable outer

135  membrane and increased sensitivity to vancomycin [27]. Our previous results showed that

136  vancomycin treatment of *imp4213* cells leads to the formation of pores in the cell wall from

137  which the inner membrane and cytoplasm eventually escape when the pore size increases

138  sufficiently [15]; before the point of this blebbing, it is difficult to detect the level of damage

139  using existing light microscopy techniques.

140

141  We treated *imp4213* cells for 10 min with 1 μg mL$^{-1}$ vancomycin; at this early time point, cells

142  did not exhibit any morphological changes due to drug treatment. Unlike untreated controls that

143  remained unexpanded (**Fig. 2A**), expansion of vancomycin-treated *imp4213* cells showed a

144  striking pattern: surrounding the unexpanded cytoplasm (GFP-labeled) was a halo of DNA (TO-

145  PRO-3-labeled) that occupied a space with width ~4 times that of an unexpanded cell (**Fig.**

146  **2B,C**). We interpret this pattern as the translocation of DNA through pores in the cell wall during

7

147 expansion (**Fig. 2D**). As the hydrogel network contained within the cell wall is unable to expand

148 with the surrounding network, an extracellular cavity with low-density networks is created that

149 lowers the effective chemical potential and drives the DNA to spread into this cavity (**Fig. 2E**).

150 We estimate the minimum chemical potential difference required for the spontaneous

151 translocation of *E. coli* DNA to be ~0.5 $k_BT$ (**Materials and Methods**), which is comparable to

152 the thermal energy. This calculation indicates that the DNA translocation is a sensitive measure

153 of cell-wall damage, as the DNA chain should always escape the confinement of the cell wall as

154 long as the pore size grows to ~100 nm (the Kuhn length of DNA). The size of these pores would

155 be below the diffraction limit, and thus invisible using conventional optical approaches.

156

157 **μExM resolves bacterial species within a model animal gut microbiota**

158 To demonstrate the utility of expansion as an imaging contrast, we focused on two applications:

159 (1) *in vivo* imaging to resolve bacterial species in an animal gut, particularly when strain-specific

160 fluorescent tags may not be available or are limited by host tissue autofluorescence (**Fig. 3**), and

161 (2) detection of cell wall disruption *in situ* when pathogenic bacteria are under attack from host

162 defense mechanisms (**Fig. 4**). In both cases, traditional spectral contrast in fluorescence

163 microscopy would be insufficient, and μExM reveals new biological insights.

164

165 First, we colonized the gut of a model organism, the planarian flatworm *Schmidtea mediterranea*

166 [28]*,* with *E. coli* and *L. plantarum*, both expressing mCherry (**S2 Fig.**). Use of mCherry was

167 prudent as planarian tissues have strong autofluorescence below 560 nm, limiting the utility of

168 other fluorescent proteins such as GFP or YFP that spectrally overlap with the autofluorescence.

169 The bacteria were introduced by feeding the planarian with a calf liver-bacteria mixture, after

170   which colonization was allowed to stabilize for 3 days (**Fig. 3A**). The planarians were then fixed

171   and imaged using the μExM protocol optimized for the planarian tissues (**S3 Fig.**).

172

173   Before expansion, bacterial cells in the planarian gut were barely resolvable (**Fig. 3B,C**).

174   Expansion clearly revealed the borders of individual cells, as distances between cells increased

175   (**Fig. 3D** and **S3 Fig.**) and the optical clearing of planarian tissues improved the signal-to-noise

176   ratio (**S3 Fig.**). Moreover, the two species became distinguishable after lysozyme treatment and

177   expansion (**Fig. 3E**); individual cell widths split into two populations corresponding to *E. coli* (2-

178   fold expanded) and *L. plantarum* (approximately unexpanded) (**Fig. 3F**, left). Single-species *in*

179   *vivo* controls verified that there is little to no overlap between the two populations (**Fig. 3F**,

180   right), with expansion ratios consistent with the *in vitro* measurements (**Fig. 1B**). We quantified

181   the relative abundance of the two species early during colonization, which correlated well with

182   that of the initial mixtures fed to the planarians (**Fig. 3G**). Together, this application

183   demonstrates that μExM can provide quantitative measures of species composition of gut

184   microbiomes, which is critical to resolve the key factors determining these compositions [24,29].

185

186   **μExM reveals previously unrecognized cell-to-cell phenotypic heterogeneity among**

187   **pathogenic bacteria during infection**

188   Next, we investigated *Salmonella* cells during macrophage infection. The fate of *Salmonella*

189   after entering macrophages is known to be heterogeneous: some cells survive and proliferate,

190   whereas others lyse in the harsh intracellular environment [30–32]. Previous studies have

191   suggested that variations in *Salmonella* cell wall structure may play an important role in

9

192   heterogeneous infection outcomes [33], but it has been challenging to measure such phenotypic

193   variations *in situ*.

194

195   We used μExM to image GFP-*Salmonella* cells engulfed by RAW264.7 macrophages, co-

196   staining DNA with DAPI. We observed two types of heterogeneity. First, expansion of

197   individual *Salmonella* cells exhibited two distinct states (**Fig. 4A,B**): some cells remained

198   unexpanded, indicative of an intact cell wall consistent with our *in vitro* experiments (**S4 Figure**),

199   whereas others exhibited an expansion pattern similar to *E. coli imp4213* cells after vancomycin

200   treatment (**Fig. 2**), indicative of nanometer-sized pores in the cell wall through which DNA

201   escaped during expansion to form a halo around the unexpanded cytoplasm (**Fig. 4C**). Second,

202   the fraction of DNA-expanded *Salmonella* cells varied drastically between individual

203   macrophages (**Fig. 4D**). The observed heterogeneity was consistent between time points post-

204   infection. These observations reveal stochasticity in the fate of *Salmonella* cells during

205   macrophage infection, the underlying mechanisms of which will be an important question for

206   future studies.

207

208   **Discussion**

209   Here, we develop an expansion microscopy method (μExM) for prokaryotes, and demonstrate

210   that expansion patterns are determined by cell-wall structural properties. We use this

211   phenomenon as a non-conventional imaging contrast, and demonstrate the utility of μExM via *in*

212   *vivo* imaging of gut microbial communities, and detection of cell-to-cell heterogeneity among

213   pathogenic bacteria as they infect macrophages. We expect this method to spur new research in

214   three major areas.

215

216 First, we have shown that in order to be applicable to microbiology, expansion microscopy must

217 be modified to predigest the bacterial cell wall with specific enzymes such as mutanolysin to

218 achieve full uniform expansion. It has been demonstrated that ExM is compatible with

219 conventional antibodies [21,25,34] and RNA fluorescence in situ hybridization [20], therefore

220 μExM is readily adaptable to image nanometer-scale ultrastructures in bacterial cells that are

221 under the diffraction limit of optical imaging. Subcellular organization in bacterial cells is a field

222 of active discovery [35], but has been so far accessible only through specialized super-resolution

223 equipment [22,36,37]. μExM should open up new applications and provide technical

224 convenience in this research area.

225

226 More importantly, beyond the established strengths of ExM (i.e., improved spatial resolution and

227 high signal-to-noise ratio), the differential expansion between cells with partially digested cell

228 walls offers a new imaging contrast that is orthogonal to spectral separation in standard

229 fluorescence microscopy using FISH probes, antibodies, or fluorescent proteins. With two

230 relevant applications (*in vivo* gut imaging and macrophage infection), we have demonstrated that

231 the contrast in expansion is quantitative and sensitive to resolve cells of different species or in

232 distinct physiological states, which are otherwise difficult to capture using traditional imaging

233 methods. As μExM requires no special microscopy instrumentation, it can be easily integrated

234 with other optical methods for high-content multimodal imaging. For example, combining

235 expansion and spectral labeling may enable concurrent identification of dozens of microbial

236 species in a complex community or to detect intermediate states as cells undergo physiological

11

237     changes. We thus anticipate μExM will have broad applications in studies of complex bacterial

238     communities in microbiota, biofilms, and at host-microbe interfaces.

239

240     Finally, while cell-wall properties may be measured using direct mechanical methods (e.g.,

241     atomic force microcopy [38] or Brillouin microscopy [39]), these methods are not applicable for

242     characterization of cells in dense populations and *in vivo* conditions. μExM can quantitatively

243     evaluate cellular phenotypes *in vivo* and *in situ* under various genetic, chemical, or physical

244     perturbations. These perturbations can include, for instance, genetic disruption of cell-wall

245     synthesis or chemical stresses such as antibiotic treatment [15,40], pH changes, and osmotic

246     shock. Future investigations will be able to compare cellular phenotypes as both isolated

247     individuals and within a dense, complex community. With the recent discovery of micro-scale

248     spatial organization in human microbiota [4,23], μExM will be a powerful tool for revealing how

249     spatial neighborhoods modulate cellular phenotypes.

250 **Materials and Methods**

251

252 *Bacterial sample preparation*

253 Bacterial strains and culture conditions used in this study are summarized in **Table 1**. For *in vitro*

254 samples, cells were collected from overnight cultures via centrifugation at 2000 $\times g$ for 5 min,

255 washed twice in PBS, and fixed in PBS containing 4% formaldehyde and 1% NP-40 for 10 min.

256 After fixation, cells were washed in PBS and then resuspended in PBST (PBS supplemented

257 with 0.3% Triton X-100) for 30 min at room temperature. The resuspended bacteria were

258 sequentially dehydrated in 50:50% methanol:PBST and then pure methanol.

259

260 For vancomycin treatment, *E. coli imp4213* cells were grown to early stationary phase ($OD_{600}$ =

261 0.8) and incubated in media containing 1 µg mL$^{-1}$ vancomycin (Sigma-Aldrich) for 10 min at 37

262 ℃ before fixation. We focused on cells during early stationary phase as we noticed large cell-to-

263 cell variations in expansion between dividing cells during exponential growth.

264

265 *Planarian sample preparation*

266 Asexual *S. mediterranea* planarians were maintained at 20 ℃ in ultrapure water supplemented

267 with 0.5 g L$^{-1}$ Instant Ocean salts and 0.1 g L$^{-1}$ NaHCO$_3$ and were fed calf liver paste once or

268 twice weekly. To colonize the planarian gut with bacteria, planarians were starved for at least 7 d,

269 then fed with 250 µL calf liver paste mixed with 50 µL of a mixture of *L. plantarum* and *E. coli*

270 cells, which were collected from 5 mL cultures in early stationary phase ($OD_{600}$ = 0.8–1.0) and

271 concentrated in 1 mL of PBS. After 3 d, individual planarians were collected into separate tubes

272 and fixed individually (to avoid clumping) in PBST containing 4% formaldehyde and 1% NP-40

13

273   for 2 h at room temperature. The fixed planarians were washed in PBST, dehydrated in 50:50%

274   methanol:PBST followed by pure methanol, and stored at -20 ℃.

275

276   To label muscle fibers using immunofluorescence, planarians were killed by 2% HCl for 5 min,

277   and then fixed in 4% formaldehyde with 1% NP-40 for 2 h at room temperature. Samples were

278   rinsed briefly in PBST and bleached overnight at room temperature with 6% $H_2O_2$ in PBST

279   under bright light. The planarians were rinsed with PBST, blocked in PBST supplemented with 1%

280   (w/v) BSA (PBSTB) for 4 h at room temperature, then incubated with the antibody 6G10 (DSHB,

281   1:1,000 dilutions in PBSTB) for 12–15 h at 4 ℃ [41]. At least 6 washes of 20 min each with

282   PBST were carried out prior to adding the peroxidase-conjugated secondary anti-mouse antibody

283   (Jackson ImmunoResearch) at a 1:1,000 dilution in PBSTB. After overnight incubation at 4 ℃,

284   samples were extensively washed in PBSTB. Tyramide signal amplification was performed by

285   incubating planarians for 10 min in homebrewed TAMRA-conjugated tyramide in 100 mM

286   borate buffer (pH = 8.5) supplemented with 2 M NaCl, 0.003% $H_2O_2$ and 20 µg mL$^{-1}$ 4-

287   iodophenylboronic acid.

288

289   *Macrophage sample preparation*

290   To infect macrophages with *Salmonella*, RAW264.7 cells were plated at 500,000 cells/well on

291   coverslips coated with fibronectin (10 µg mL$^{-1}$ for 30 min) in 6-well plates and allowed to attach

292   overnight. Cells were rinsed three times with Fluorobrite DMEM media (ThermoFisher

293   Scientific) supplemented with 10 mM HEPES, 1% FBS, and 2 mM L-glutamine. Overnight

294   cultures of *Salmonella* were diluted in Fluorobrite DMEM media and added to wells at a 1,250:1

295   multiplicity of infection (MOI). The plate was centrifuged (200 ×*g*) for 15 min at 34 ℃. Infected

14

296    macrophages were washed twice to remove extra bacteria, and 1 mL of medium containing 10

297    μg mL$^{-1}$ gentamicin was added to each well. Cells were cultured at 37 ℃ under 5% $CO_2$ for 3-9

298    h, then fixed in PBS containing 4% formaldehyde and 1% NP-40 for 10 min. After fixation, cells

299    were dehydrated in methanol and stored at -20 ℃.

300

301    ***μExM***

302    Dehydrated samples (bacterial cells, planarian tissues, infected macrophages) were kept at -20 ℃

303    for at least overnight and sequentially rehydrated with 50:50% methanol:PBST, then PBST. To

304    digest bacterial cell walls, samples were incubated overnight at 37 ℃ in either PBS containing 2

305    mg mL$^{-1}$ lysozyme (ThermoFisher Scientific) or in 50 mM phosphate buffer (pH = 4.9)

306    containing 40 μg mL$^{-1}$ mutanolysin (Sigma-Aldrich), unless otherwise specified.

307

308    After cell wall digestion, samples were rinsed three times with PBS, then incubated for 1 h in a

309    PBS solution of 1 mM methacrylic acid *N*-hydroxysuccinimide ester (MA-NHS, Sigma-Aldrich),

310    diluted from a 1 M MA-NHS DMSO stock. After rigorous washes with PBS, samples were

311    incubated in monomer solution ($1 \times$ PBS, 2 M NaCl, 8.625% (w/w) sodium acrylate, 2.5% (w/w)

312    acrylamide, 0.15% (w/w) N,N'-methylenebisacrylamide) for 1 min (bacterial cells and

313    macrophages) or 45 min (planarian tissues) at 4 ℃ before gelation.

314

315    Gelation was performed in chambers that were assembled using two coverslips as spacers placed

316    between microscope slides. Gelation was initiated by adding monomer solutions supplemented

317    with 0.2% w/w ammonium persulfate stock (10% (w/w), ThermoFisher Scientific) and

318    tetramethylethylenediamine (ThermoFisher Scientific). For planarian tissues and macrophage

319    samples, 4-hydroxy-2,2,6,6- tetramethylpiperidin-1-oxyl (4-hydroxy-TEMPO, Sigma-Aldrich)

320    was added at a concentration of 0.05% (w/w) to inhibit gelation during the diffusion of

321    monomers into tissues. Gelation was completed by incubation at 37 °C for 1-2 h.

322

323    After gelation, gels were gently removed from the chamber and digested overnight at 37 °C in 8

324    units mL$^{-1}$ Proteinase K (NEB) diluted in digestion buffer ($1\times$ TAE buffer, 0.5% Triton X-100,

325    0.8 M guanidine HCl). Gels were then removed from digestion buffer and placed in excess

326    distilled water to expand. Water was exchanged every 15 min 3-5 times until the size of the

327    expanded gels plateaued. To stain DNA, expanded samples were incubated with 100 μM DAPI

328    or 1 μM TO-PRO-3 for 30 min.

329

330    Fluorescence confocal imaging was performed on a Zeiss LSM 800 using either a $20\times$, N.A. =

331    1.0, water-immersion objective (W Plan-Apochromat) or a $40\times$, N.A. = 1.1, water-immersion

332    objective (LD C-Apochromat Corr M27). Expanded samples were mounted in imaging chambers

333    assembled from iSpacer (3.0-mm deep, Sunjin lab). To image a large area, tiled images were

334    stitched using either ZEN or FIJI. The FIJI plugin "Mosaic" was used for the segmentation of

335    bacterial cells. After segmentation, a custom MATLAB script was used to measure aspect ratio

336    and cell width. Cell width is computed along the short axis and averaged at 5 locations evenly

337    spaced along the long axis.

338

339    **Estimate of chemical potential for spontaneous translocation of DNA from cell-wall**

340    **confinement**

16

341    We model the translocation of a DNA chain through a pore in the cell wall consisting of two

342    primary steps. First, one end of the DNA is anchored near the pore. The anchoring energy and

343    the loss of conformational entropy due to the localization of the chain end gives rise to a free

344    energy barrier of the form [42]

$$\frac{F^{\dagger}}{k_{\mathrm{B}}T} = \frac{\varepsilon}{k_{\mathrm{B}}T} + \ln\left(\frac{4R^4}{\pi a v}\right),$$

345    where $\varepsilon$ is the anchoring energy, $R$ the confinement radius (essentially equivalent to the radius of

346    the cell), $a$ is the range of anchoring near the pore, and $v$ is the volume of the anchored segment.

347    This free energy barrier must be overcome to initialize translocation. Since the anchoring energy

348    depends on the details of the pore and the way it interacts with the anchored segment, it is

349    impractical to evaluate exactly the numerical value of this barrier. Nonetheless, it is apparent that

350    stronger confinement (smaller $R$) lowers the barrier height. Moreover, the presence of multiple

351    pores in the cell wall that are sufficiently large for translocation increases the probability that the

352    DNA is anchored at such a pore.

353

354    The second step concerns the actual translocation. After anchored, the DNA chain diffuses along

355    its backbone, outwards or inwards, across the pore. At any instant, one particular segment,

356    labeled $m$, is anchored at the pore, reducing the conformational entropy of the DNA chain (**Fig.**

357    **2D**). By treating the chain as a Gaussian random walk, the free energy associated with this

358    entropy loss can be obtained in terms of a series summation [43]. In the limit of strong

359    confinement (i.e., when $R$ is smaller than the radius of gyration of the DNA, $R_g$), the ground-state

360    dominance approximation [42] leads to the following expression for the free energy as a function

361    of $m$:

17

$$\frac{F(m)}{k_\mathrm{B}T} = -\ln\left[1 + \frac{R}{R_\mathrm{g}}\left(\frac{N}{\pi m}\right)^{\frac{1}{2}}\right] + \frac{\pi^2(N-m)}{N}\left(\frac{R_\mathrm{g}}{R}\right)^2 + m\frac{\Delta\mu}{k_\mathrm{B}T},$$

362    where $N$ is the total number of segments and $\Delta\mu$ is the difference in chemical potential of each

363    segment outside and inside the cell. The first and the second terms come from the conformational

364    entropies of the two half-chains outside and inside the cell, respectively. Note that the free

365    energy depends on the confinement through the ratio $R/R_\mathrm{g}$.

366

367    We evaluated the free energy difference $\Delta F(m) \equiv F(m) - F(1)$ (**Fig. 2E**) for the nucleoid

368    confined inside a bacterial cell. We set the radius of the cell to be $R = 1$ μm, and the length of

369    DNA to be that of *E. coli*. The *E. coli* genome is 4.7 Mbp, having a contour length $L$ of 1.596

370    mm. Using 1 nm as the radius of the cross section, we estimate that the DNA fills ~0.1% of the

371    intracellular volume, and hence crowding should not substantially hinder segmental motions.

372    Estimating the Kuhn length of DNA at $l_\mathrm{K} = 100$ nm, we find the number of Kuhn segments $N =$

373    $L/l_\mathrm{K} = 15{,}980$ and the radius of gyration $R_\mathrm{g} = N^{1/2}l_\mathrm{K} = 5.2$ μm. As a result, the DNA is strongly

374    confined, with $R/R_\mathrm{g} = 0.19$.

375

376    The salient feature of our model across chemical potential differences $\Delta\mu$ is the existence of a

377    single, *entropic* barrier for molecular translocation (**Fig. 2E**). This barrier originates from the

378    entropy loss associated with translocating the first few segments outside the pore, in addition to

379    those originally anchored inside. Once this entropic barrier is overcome, the free energy decays

380    monotonically with $m$, and DNA translocation proceeds spontaneously. Differentiating the free

381    energy leads to a cubic equation for the location of the barrier, $m^*$, which shows that $m^*$ depends

382    on the confinement size $R/l_\mathrm{K}$ and on the chemical potential difference $\Delta\mu$, but *not* on the DNA

18

383    length $N$. In particular, for $\Delta\mu = 0$, $m^* = 0.23(R/l_K)^2$; in this case, for $R = 1$ μm, $m^* = 23$,

384    indicating that 23 Kuhn segments (equivalent to ~6.7 kbp) need to be successfully translocated

385    via diffusive curvilinear motion before the whole chain spontaneously escapes the confinement.

386

387    Lowering the segmental chemical potential outside the cell reduces $m^*$ and lowers the height of

388    the barrier (**Fig. 2E**). As external localization becomes sufficiently friendly (lower $\Delta\mu$), the

389    entropic barrier may disappear altogether. By setting $m^* = 1$, we identified that such a transition

390    occurs when

$$\Delta\mu \le \Delta\mu_c = \left[\frac{\pi}{z_c^2} - \frac{z_c}{2(1 + z_c)}\right]k_B T, \qquad z_c = \left(\frac{6}{\pi}\right)^{\frac{1}{2}}\frac{R}{l_K}.$$

391    For $R/l_K = 10$, $\Delta\mu_c = -0.45$ $k_B T$ is the chemical potential at which the energy barrier for DNA

392    translocation vanishes.

393

20

## References

1.  Donaldson GP, Lee SM, Mazmanian SK. Gut biogeography of the bacterial microbiota. Nat Rev Microbiol. 2016;14: 20–32. doi:10.1038/nrmicro3552

2.  Earle KA, Billings G, Sigal M, Lichtman JS, Hansson GC, Elias JE, et al. Quantitative imaging of gut microbiota spatial organization. Cell Host Microbe. 2015;18: 478–488. doi:10.1016/j.chom.2015.09.002

3.  Tropini C, Earle KA, Huang KC, Sonnenburg JL. The Gut microbiome: Connecting spatial organization to function. Cell Host Microbe. 2017;21: 433–442. doi:10.1016/j.chom.2017.03.010

4.  Mark Welch JL, Hasegawa Y, McNulty NP, Gordon JI, Borisy GG. Spatial organization of a model 15-member human gut microbiota established in gnotobiotic mice. Proc Natl Acad Sci USA. 2017;114: E9105–E9114. doi:10.1073/pnas.1711596114

5.  Whitaker WR, Shepherd ES, Sonnenburg JL. Tunable expression tools enable single-cell strain distinction in the gut microbiome. Cell. 2017;169: 538–546. doi:10.1016/j.cell.2017.03.041

6.  Tropini C, Moss EL, Merrill BD, Ng KM, Higginbottom SK, Casavant EP, et al. Transient osmotic perturbation causes long-term alteration to the gut microbiota. Cell. 2018;173: 1742–1754. Epub 2018/06/16. doi:10.1016/j.cell.2018.05.008

7.  Reese AT, Pereira FC, Schintlmeister A, Berry D, Wagner M, Hale LP, et al. Microbial nitrogen limitation in the mammalian large intestine. Nat Microbiol. 2018;3: 1441–1450. doi:10.1038/s41564-018-0267-7

8.  Matias VRF, Beveridge TJ. Cryo-electron microscopy reveals native polymeric cell wall structure in Bacillus subtilis 168 and the existence of a periplasmic space. Mol Microbiol. 2005;56: 240–251. doi:10.1111/j.1365-2958.2005.04535.x

9.  Misra G, Rojas ER, Gopinathan A, Huang KC. Mechanical consequences of cell-wall turnover in the elongation of a Gram-positive bacterium. Biophys J. 2013;104:2342–2352. doi:10.1016/j.bpj.2013.04.047

10. Gan L, Chen S, Jensen GJ. Molecular organization of Gram-negative peptidoglycan. Proc Natl Acad Sci USA. 2008;105:18953–18957. doi:10.1073/pnas.0808035105

11. Tuson HH, Auer GK, Renner LD, Hasebe M, Tropini C, Salick M, et al. Measuring the stiffness of bacterial cells from growth rates in hydrogels of tunable elasticity. Mol Microbiol. 2012;84: 874–891. doi:10.1111/j.1365-2958.2012.08063.x

12. Yao X, Jericho M, Pink D, Beveridge T. Thickness and elasticity of Gram-negative *Murein sacculi* measured by atomic force microscopy. J Bacteriol. 1999;181: 6865–6875.

13. Desmarais SM, De Pedro MA, Cava F, Huang KC. Peptidoglycan at its peaks: how chromatographic analyses can reveal bacterial cell wall structure and assembly. Mol Microbiol. 2013;89: 1–13. doi:10.1111/mmi.12266

14. Sycuro LK, Pincus Z, Gutierrez KD, Biboy J, Stern CA, Vollmer W, et al. Peptidoglycan crosslinking relaxation promotes *Helicobacter pylori*'s helical shape and stomach colonization. Cell. 2010;141: 822–833. doi:10.1016/j.cell.2010.03.046

15.  Huang KC, Mukhopadhyay R, Wen B, Gitai Z, Wingreen NS. Cell shape and cell-wall organization in Gram-negative bacteria. Proc Natl Acad Sci USA. 2008;105: 19282–19287. doi:10.1073/pnas.0805309105

16.  Baranowski C, Welsh MA, Sham L-T, Eskandarian HA, Lim HC, Kieser KJ, et al. Maturing *Mycobacterium smegmatis* peptidoglycan requires non-canonical crosslinks to maintain shape. eLife. 2018;7: e37516. doi:10.7554/eLife.37516

17.  Turner RD, Hobbs JK, Foster SJ. Atomic force microscopy analysis of bacterial cell wall peptidoglycan architecture. In: Hong H-J, editor. Bacterial cell wall homeostasis: Methods and protocols. New York, NY: Springer New York; 2016. pp. 3–9.

18.  Zhang YS, Chang J-B, Alvarez MM, Trujillo-de Santiago G, Aleman J, Batzaya B, et al. Hybrid microscopy: Enabling inexpensive high-performance imaging through combined physical and optical magnifications. Sci Rep. 2016;6: 22691. doi:10.1038/srep22691

19.  Chen F, Tillberg PW, Boyden ES. Expansion microscopy. Science. 2015;347: 543–548. doi:10.1126/science.1260088

20.  Chen F, Wassie AT, Cote AJ, Sinha A, Alon S, Asano S, et al. Nanoscale imaging of RNA with expansion microscopy. Nat Methods. 2016;13: 679–684. doi:10.1038/nmeth.3899

21.  Tillberg PW, Chen F, Piatkevich KD, Zhao Y, Yu C-C (Jay), English BP, et al. Protein-retention expansion microscopy of cells and tissues labeled using standard fluorescent proteins and antibodies. Nat Biotechnol. 2016;34: 987–992. doi:10.1038/nbt.3625

22.  Coltharp C, Xiao J. Superresolution microscopy for microbiology. Cell Microbiol. 2012;14:1808–1818. doi:10.1111/cmi.12024

23.  Mark Welch JL, Rossetti BJ, Rieken CW, Dewhirst FE, Borisy GG. Biogeography of a human oral microbiome at the micron scale. Proc Natl Acad Sci USA. 2016;113:E791–E800. doi:10.1073/pnas.1522149113

24.  Obadia B, Güvener ZT, Zhang V, Ceja-Navarro JA, Brodie EL, Ja WW, et al. Probabilistic invasion underlies natural gut microbiome stability. Curr Biol. 2017;27: 1999–2006. doi:10.1016/j.cub.2017.05.034

25.  Chozinski TJ, Halpern AR, Okawa H, Kim H-J, Tremel GJ, Wong ROL, et al. Expansion microscopy with conventional antibodies and fluorescent proteins. Nat Methods. 2016;13: 485–488. doi:10.1038/nmeth.3833

26.  Yuan S, Cohen DB, Ravel J, Abdo Z, Forney LJ. Evaluation of methods for the extraction and purification of DNA from the human microbiome. PLoS One. 2012;7: e33865. doi:10.1371/journal.pone.0033865

27.  Wu T, Malinverni J, Ruiz N, Kim S, Silhavy TJ, Kahne D. Identification of a multicomponent complex required for outer membrane biogenesis in *Escherichia coli*. Cell. 2005;121: 235–245. doi:10.1016/j.cell.2005.02.015

28.  Arnold CP, Merryman MS, Harris-Arnold A, McKinney SA, Seidel CW, Loethen S, et al. Pathogenic shifts in endogenous microbiota impede tissue regeneration via distinct activation of TAK1/MKK/p38. eLife. 2016;5: e16793. doi:10.7554/eLife.16793

29. Vega NM, Gore J. Stochastic assembly produces heterogeneous communities in the *Caenorhabditis elegans* intestine. PLoS Biol. 2017;15: e2000633. doi:10.1371/journal.pbio.2000633

30. Helaine S, Thompson JA, Watson KG, Liu M, Boyle C, Holden DW. Dynamics of intracellular bacterial replication at the single cell level. Proc Natl Acad Sci USA. 2010;107: 3746–3751. doi:10.1073/pnas.1000041107

31. Saliba A-E, Li L, Westermann AJ, Appenzeller S, Stapels DAC, Schulte LN, et al. Single-cell RNA-seq ties macrophage polarization to growth rate of intracellular *Salmonella*. Nat Microbiol. 2017;2: 16206. doi:10.1038/nmicrobiol.2016.206

32. Rycroft JA, Gollan B, Grabe GJ, Hall A, Cheverton AM, Larrouy-Maumus G, et al. Activity of acetyltransferase toxins involved in Salmonella persister formation during macrophage infection. Nat Commun. 2018;9: 1993. doi:10.1038/s41467-018-04472-6

33. Nakano M, Saito K. Chemical components in the cell wall of *Salmonella typhimurium* affecting its virulence and immunogenicity in mice. Nature. 1969;222: 1085–1086. doi:10.1038/2221085a0

34. Gambarotto D, Zwettler FU, Le Guennec M, Schmidt-Cernohorska M, Fortun D, Borgers S, et al. Imaging cellular ultrastructures using expansion microscopy (U-ExM). Nat Methods. 2019;16: 71–74. doi:10.1038/s41592-018-0238-1

35. Surovtsev I V., Jacobs-Wagner C. Subcellular organization: A critical feature of bacterial cell replication. Cell. 2018;172: 1271–1293. doi:10.1016/j.cell.2018.01.014

36. Bayas CA, Wang J, Lee MK, Schrader JM, Shapiro L, Moerner WE. Spatial organization and dynamics of RNase E and ribosomes in Caulobacter crescentus. Proc Natl Acad Sci USA. 2018;115: E3712–E3721. doi:10.1073/pnas.1721648115

37. Fei J, Singh D, Zhang Q, Park S, Balasubramanian D, Golding I, et al. Determination of in vivo target search kinetics of regulatory noncoding RNA. Science. 2015;347: 1371–1374. doi:10.1126/science.1258849

38. Rojas ER, Billings G, Odermatt PD, Auer GK, Zhu L, Miguel A, et al. The outer membrane is an essential load-bearing element in Gram-negative bacteria. Nature. 2018;559: 617–621. doi:10.1038/s41586-018-0344-3

39. Diz-Muñoz A, Weiner OD, Fletcher DA. In pursuit of the mechanics that shape cell surfaces. Nat Phys. 2018;14: 648–652. doi:10.1038/s41567-018-0187-8

40. Coates J, Park BR, Le D, Şimşek E, Chaudhry W, Kim M. Antibiotic-induced population fluctuations and stochastic clearance of bacteria. eLife. 2018;7: e32976. doi:10.7554/eLife.32976

41. Ross KG, Omuro KC, Taylor MR, Munday RK, Hubert A, King RS, et al. Novel monoclonal antibodies to study tissue regeneration in planarians. BMC Dev Biol. 2015;15: 2. doi:10.1186/s12861-014-0050-9

42. Muthukumar M. Ploymer Translocation. 1st ed. CRC Press; 2011.

43. Park PJ, Sung W. Polymer release out of a spherical vesicle through a pore. Phys Rev E. 1998;57: 730–734. doi:10.1103/PhysRevE.57.730

23

523 **Table 1: Expansion of bacteria is species specific.**

524

| Strains[1] | Culture medium[3] | Culture condition | Antibiotic resistance | Expansion ratio[4] |
|---|---|---|---|---|
| *Lactobacillus plantarum* | MRS | Aerobic, 30 ℃ | chloramphenicol | $1.12 \pm 0.03$ |
| *Acetobacter tropicalis* | MRS | Aerobic, 30 ℃ | tetracycline | $3.09 \pm 0.07$ |
| *Escherichia coli* | LB | Aerobic, 37 ℃ | ampicillin | $2.21 \pm 0.04$ |
| *E. coli imp4213* | LB | Aerobic, 37 ℃ | kanamycin | N.D. |
| *Salmonella enterica (SL12023)* | LB | Aerobic, 37 ℃ | ampicillin | $2.23 \pm 0.05$ |
| *Bifidobacterium breve*[2] | RCM | Anaerobic, 37 ℃ | N.A. | $1.21 \pm 0.04$ |
| *Clostridium innocuum*[2] | RCM | Anaerobic, 37 ℃ | N.A. | $1.14 \pm 0.03$ |
| *Acidaminococcus intestini*[2] | GAM | Anaerobic, 37 ℃ | N.A. | $3.98 \pm 0.09$ |
| *Bacteroides finegoldii*[2] | GAM | Anaerobic, 37 ℃ | N.A. | $3.67 \pm 0.07$ |
| *Parabacteroides distasonis*[2] | GAM | Anaerobic, 37 ℃ | N.A. | $3.79 \pm 0.09$ |

525

526 [1] magenta, Gram-positive; green, Gram-negative.

527 [2] obtained through BEI Resources, NIAID, NIH, as part of the Human Microbiome Project:

528 *Bifidobacterium breve* strain HPH0326, HM-856; *Clostridium innocuum* strain 6_1_30, HM-173;

529 *Acidaminococcus intestini* strain D21, HM-81; *Bacteroides finegoldii* strain CL09T03C10, HM-

530 727; *Parabacteroides distasonis* strain 31_2, HM-169 (previously deposited as *Porphyromonas*

531 sp.).

532 [3] MRS, De Man, Rogosa, and Sharpe; LB, Lysogeny Broth; RCM, Reinforced Clostridial

533 Medium; GAM, Gifu Anaerobic Medium.

534    [4] The expansion ratio is computed as the average cell width in post-expansion images divided by

535    the average cell width in pre-expansion images of lysozyme-treated cells, and reported as mean $\pm$

536    SEM (standard error of the mean).

**Figures**
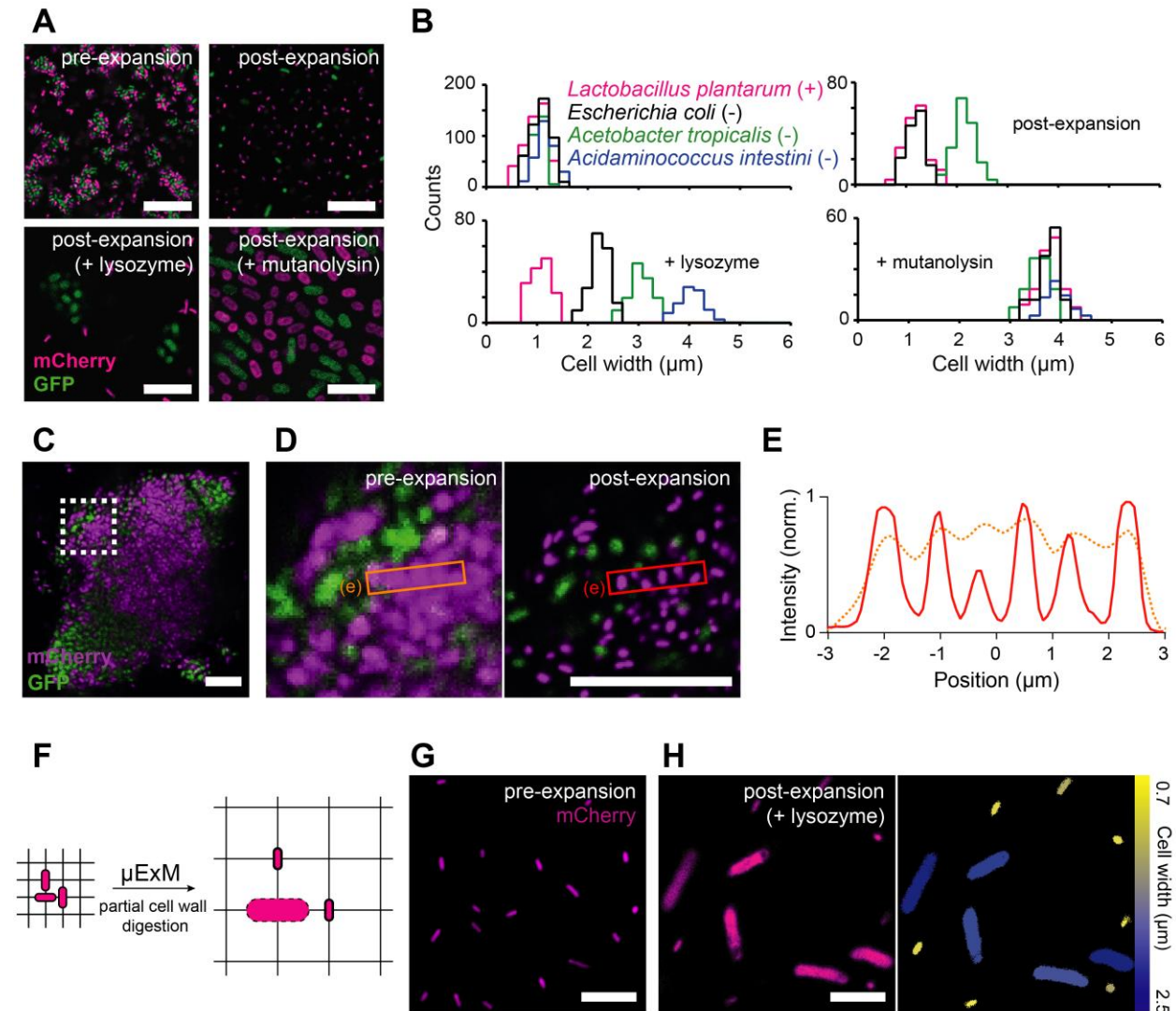


**Figure 1: Differential expansion provides novel imaging contrast in μExM.** (A) Representative confocal fluorescence images of mCherry-*L. plantarum* and GFP-*A. tropicalis* in close proximity. Top: untreated cells pre- and post-expansion; bottom left: cells treated with lysozyme to partially digest the bacterial cell wall before expansion; bottom right: cells treated with mutanolysin to fully digest the cell wall before expansion. (B) Quantification of cell width before and after expansion for representative microbial species. Lysozyme treatment maximizes

546   the contrast in expansion between species, while mutanolysin treatment expands all species ~4-

547   fold. When fluorescently labeled strains were not available, we measured the expansion ratio

548   using DNA staining. "(+)" and "(-)" denote Gram-positive and Gram-negative, respectively. (C)

549   Pre-expansion image of a colony of mCherry-*L. plantarum* and GFP-*A. tropicalis*. (D) Magnified

550   view of the boxed region in (C) before expansion (left) and after mutanolysin treatment and

551   expansion (right). The scale bar in the post-expansion image is rescaled to match the pre-

552   expansion dimension. (E) Cross-sectional normalized fluorescence intensity profiles of the boxed

553   regions in (D), showing that μExM preserves the relative positions of cells (peaks in the orange

554   and red curves overlap). (F) Schematic showing that differential expansion provides imaging

555   contrast to distinguish microbial species in mixed populations. (G) Pre-expansion image of a

556   mixture of mCherry-*L. plantarum* and mCherry-*E. coli*. The species have approximately the

557   same dimensions, making them hard to distinguish. (H) μExM easily distinguishes *L. plantarum*

558   and *E. coli* based on expansion ratio. Left: confocal image; right: the corresponding image false-

559   colored by cell width. *E. coli* cells are expanded (blue) whereas *L. plantarum* cells remain

560   unexpanded (yellow). All images are maximum intensity projections. Scale bars: 10 μm.
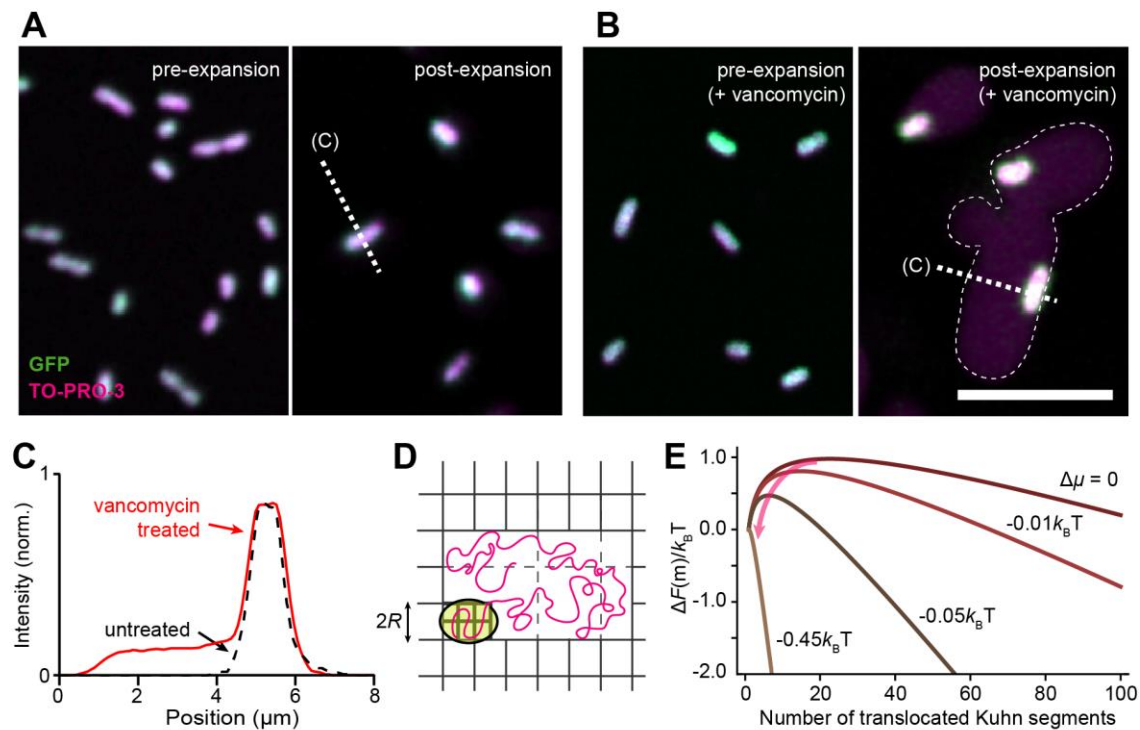
**Figure 2: µExM detects with high sensitivity cell-wall damage induced by antibiotics.** (A) Images of GFP-expressing *imp4213 E. coli* cells, with DNA co-stained using TO-PRO-3, before (left) and after (right) expansion. (B) Images of vancomycin-treated *imp4213* cells, in which expansion leads to a large halo of DNA fluorescence surrounding the unexpanded cytoplasm. All images are maximum intensity projections. Scale bars: 10 µm. (C) Normalized intensity profiles of TO-PRO-3 fluorescence measured along dashed lines in (A) and (B). (D) Proposed mechanism of DNA expansion through the translocation of a DNA chain. Yellow: cytoplasm; magenta: DNA; grey: gel network. Note the high-density gel network in the cell and low-density network around the cell. (E) The free energy for DNA translocation, $\Delta F(m)$, as a function of $m^{\text{th}}$ Kuhn segment anchored at the pore. $\Delta F(m)$ has a maximum at $m^*$, which presents an entropic barrier for DNA translocation The lower density outside the cell wall due to expansion leads to a negative chemical potential difference ($\Delta\mu$), which facilitates the translocation process by

28

574      reducing $m^*$ (arrow) and eventually causes the entropic barrier to vanish ($\Delta\mu <$ -0.45 $k_{\mathrm{B}}T$) for

575      spontaneous DNA translocation.
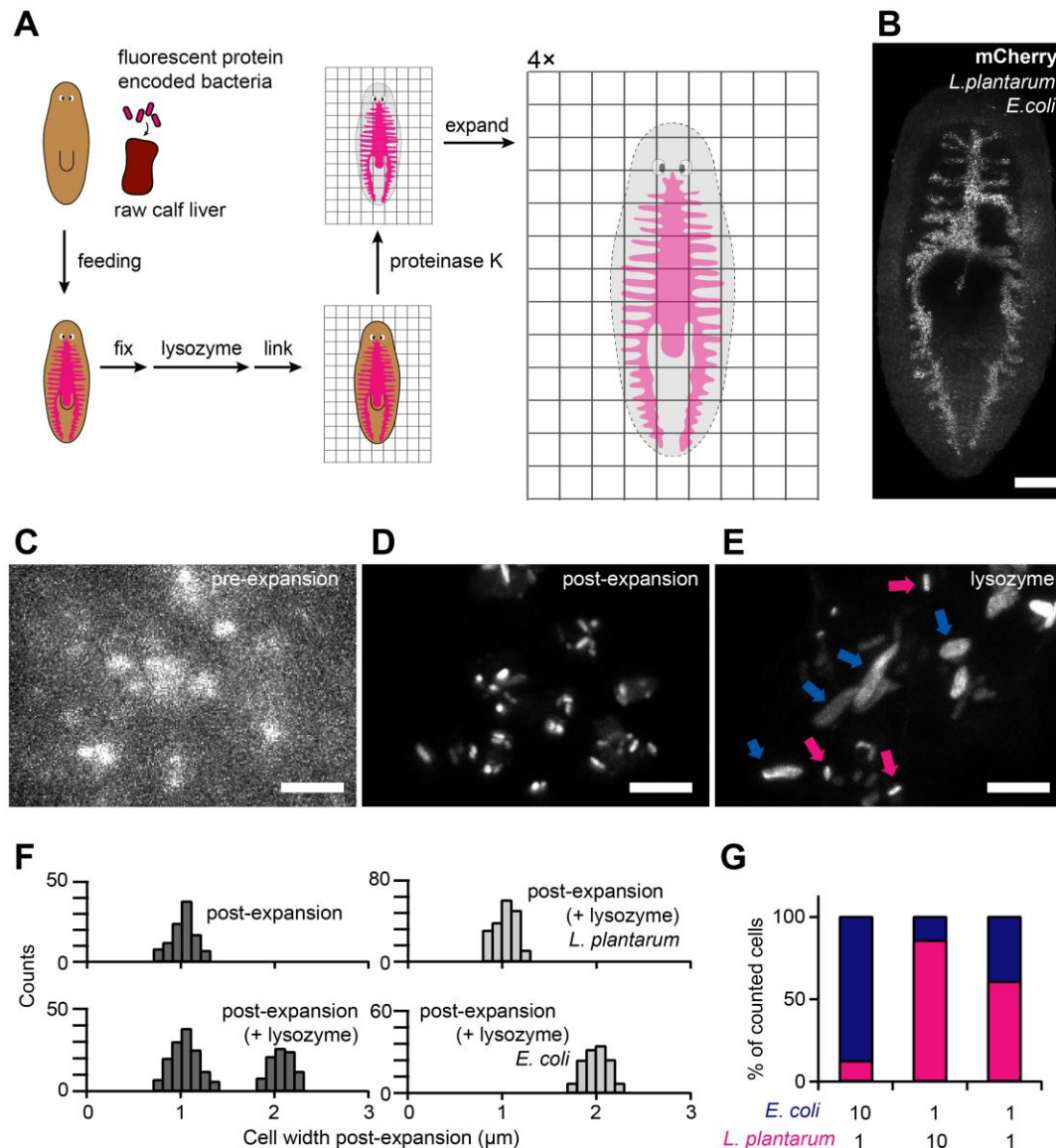
**Figure 3: μExM resolves different bacterial species in the planarian flatworm gut.** (A) Schematic of the μExM workflow for planarians. Planarians were fed with fluorescent bacteria, and fixed. Unlike other ExM protocols, μExM uses lysozyme or mutanolysin to digest the bacterial cell wall. Linker molecules were then used to anchor the planarian tissue as well as microbial proteins to the hydrogel network. After digestion with proteinase K, the hydrogel was expanded 4-fold isotropically. (B) Pre-expansion maximum-intensity projection of a planarian with its gut colonized by a mixture of *E. coli* and *L. plantarum*, both expressing mCherry.

584    Imaging was performed at 3 d after feeding the planarian with microbes. Scale bar: 200 μm. (C-

585    E) Magnified views showing microbial populations before expansion (C), after expansion (D),

586    and after expansion with lysozyme treatment (E). In (E), magenta arrows indicate unexpanded

587    cells (*L. plantarum*) and blue arrows indicate expanded cells (*E. coli*). Scale bars: 10 μm. (F)

588    Quantification of cell width of the mixed populations of *E. coli* and *L. plantarum* in the planarian

589    gut (left). Right: *In vivo* control populations containing a single species. (G) Species composition

590    in the planarian gut at 3 d post-feeding, counted based on cell width after lysozyme treatment

591    and expansion. *n*>250 cells were measured for each condition. The relative abundance of the two

592    species in the initial mixture fed to the planarians is shown below the plot.

593
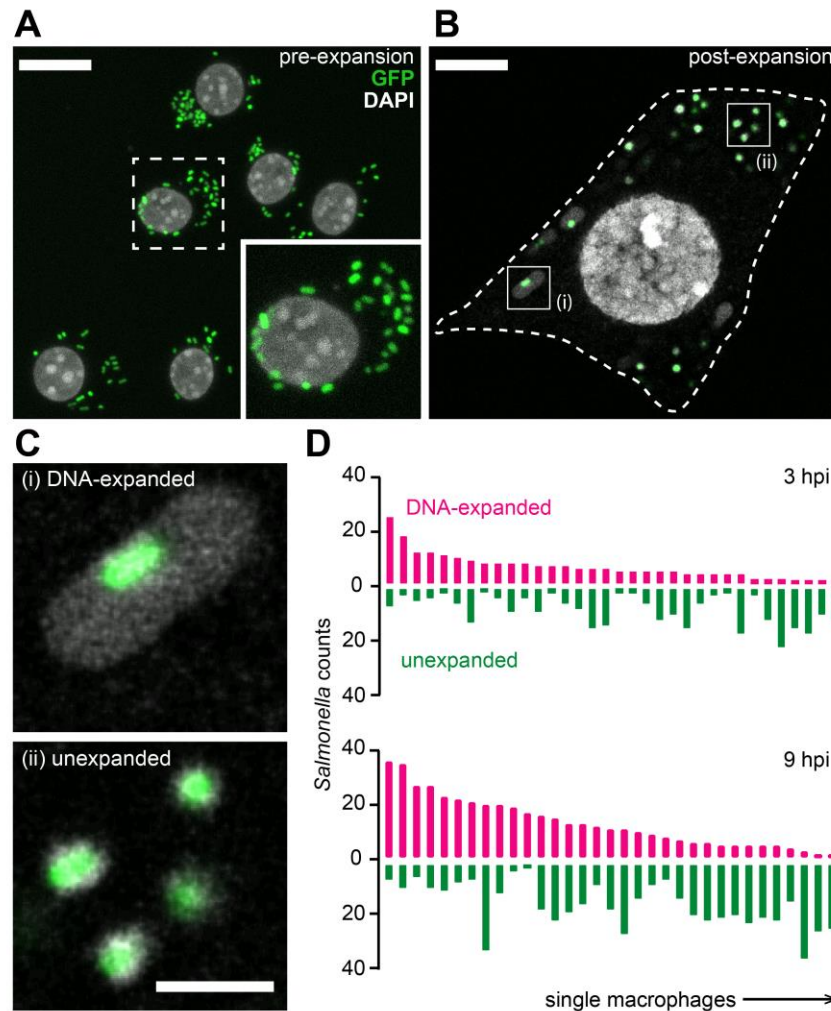
**Figure 4: μExM detects changes in the cell-wall structure of macrophage-engulfed *Salmonella* cells.** (A,B) Confocal images of RAW264.7 cells infected with GFP-*Salmonella* 3 h post infection before (A) and after (B) expansion. Inset in (A): magnified view of the boxed area. Dashed line in (B): macrophage periphery. Scale bars: 20 μm. (C) Magnified views showing two populations of *Salmonella*: DNA-expanded (top) and unexpanded (bottom), corresponding to cells highlighted by boxes in (B). Scale bar: 5 μm. (D) Number of expanded and unexpanded *Salmonella* cells in individual macrophages determined by manual counting at 3 h (top) and 9 h (bottom) post-infection (hpi). Note that the numbers of both types increase with time as *Salmonella* cells proliferate.

603 **Supplementary Figures**

604
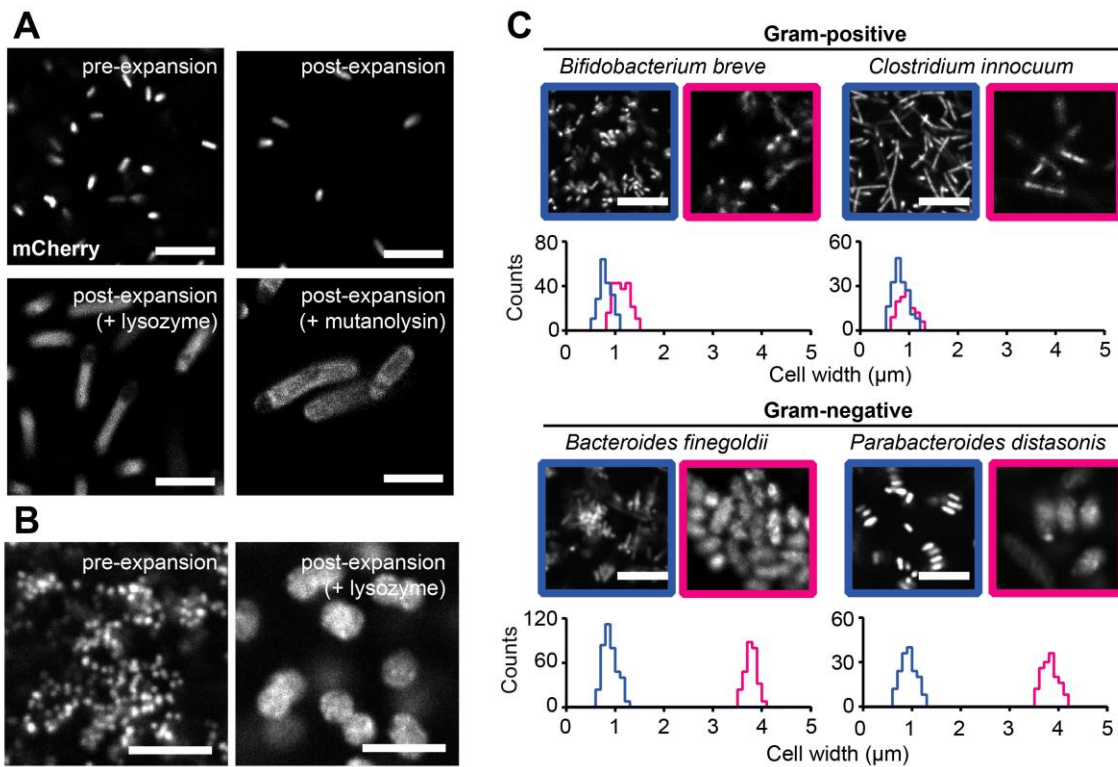


606 **S1 Figure: µExM expands microbial species to different extents.** (A) Representative µExM

607 images of mCherry-*E. coli*. Corresponding quantifications of cell width with the various

608 treatments are shown in **Fig. 1B**. (B) µExM images of *Acidaminococcus intestini*, with DNA

609 stained using TO-PRO-3. Corresponding quantifications of cell width are shown in **Fig. 1B**. (C)

610 Representative µExM images of various human commensal bacterial species. DNA was stained

611 with TO-PRO-3. Blue: pre-expansion images; magenta: post-expansion images after lysozyme

612 treatment. Corresponding quantifications of cell width are shown under the images. All Images

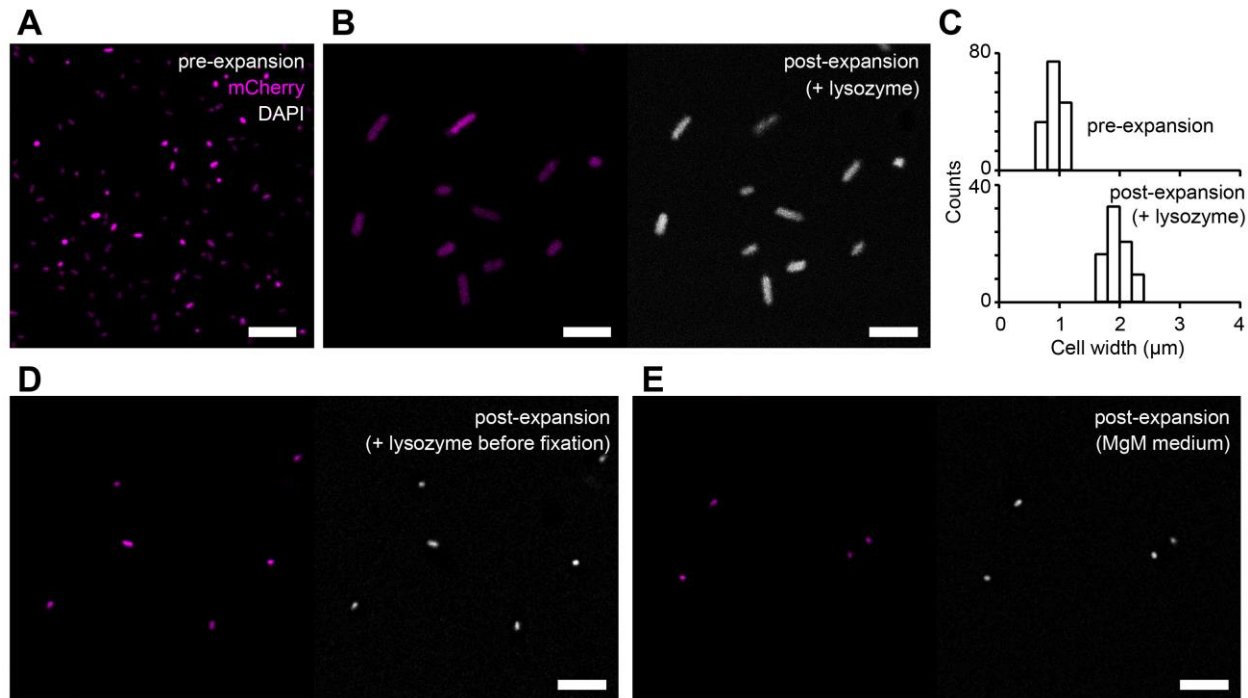613 are maximum intensity projections. Scale bars: 10 µm.

614
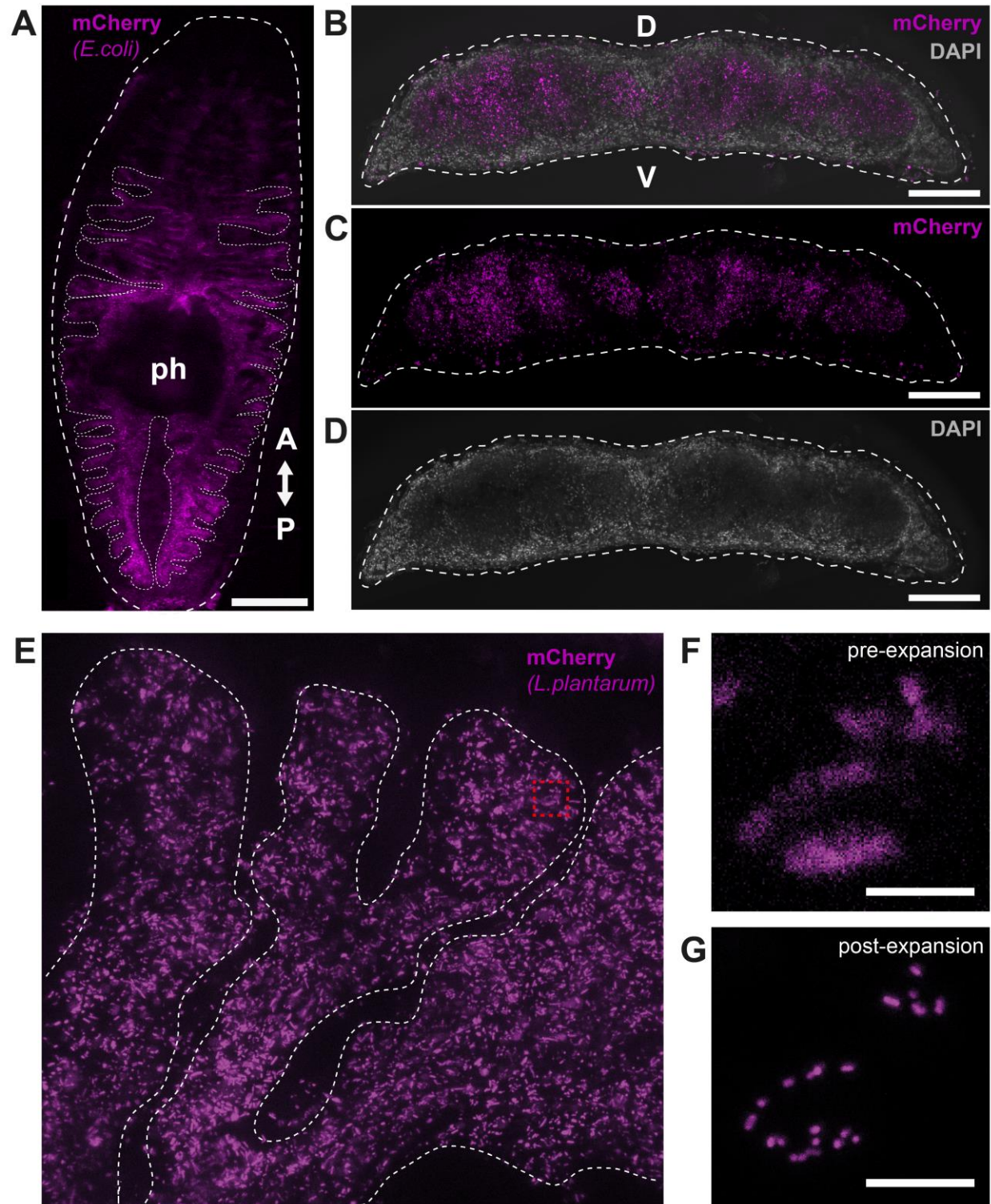
**S2 Figure: Imaging of fluorescent bacteria colonizing the planarian gut.** (A) Confocal image

showing a whole planarian, fed with mCherry-*E. coli*, at 3 d post-feeding. The planarian gut and

34

617    its branches (dotted line) are clearly visible. A, anterior; P, posterior. Scale bar: 500 μm. (B-D)

618    Transverse sections of the planarian trunk region showing that fluorescent *E. coli* are primarily

619    located inside the planarian gut. Dashed line: the outline of the planarian body. D, dorsal; V,

620    ventral. Scale bars: 200 μm. (E) A representative section of the planarian gut colonized by

621    mCherry-*L. plantarum*, at 3 d post-feeding. Dashed line: the outline of gut branches. (F,G)

622    Magnified views of the highlighted region (red square) in (E), before (F) and after expansion (G).

623    Without cell-wall digestion, *L. plantarum* cells remained unexpanded, but the distances between

624    cells increased 4-fold, allowing single cells to be optically resolved. Scale bars: 10 μm. All

625    images are maximum intensity projections.

626
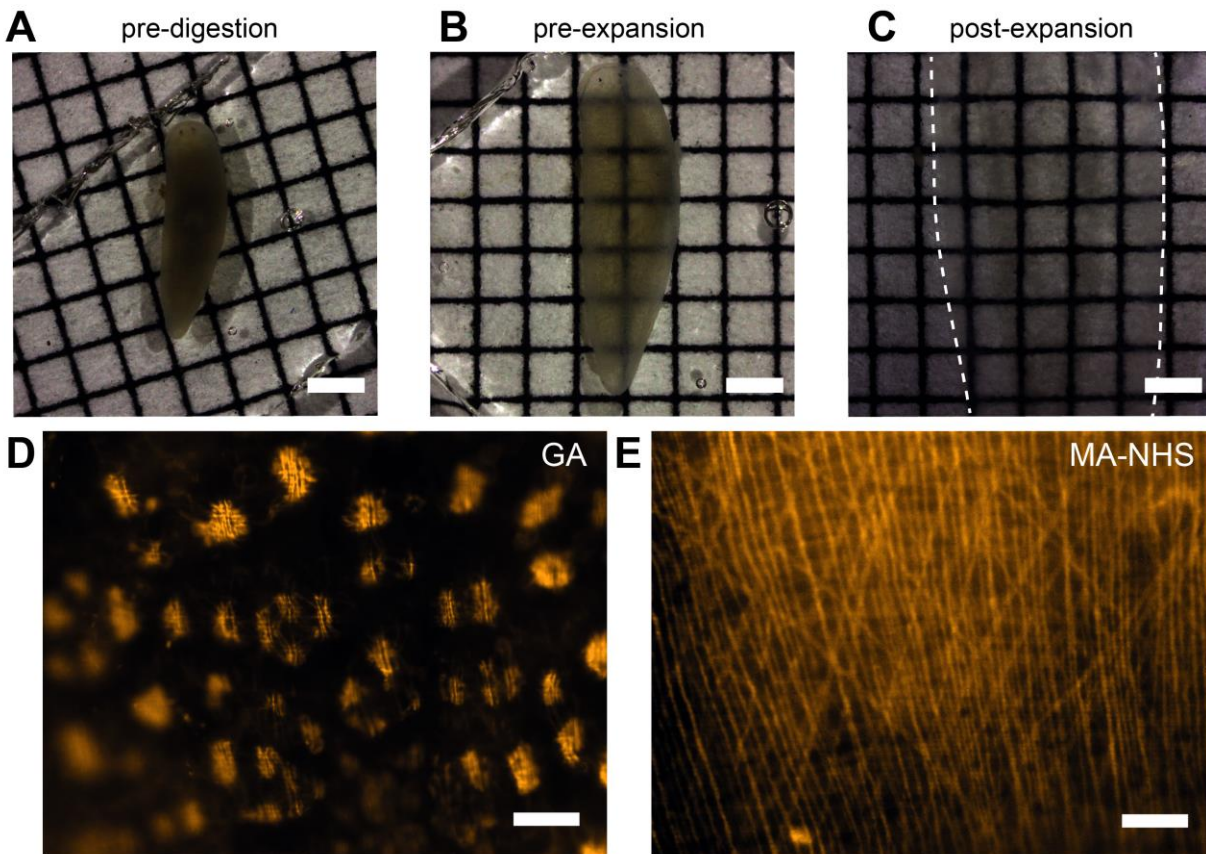
**S3 Figure: Optimization of μExM for planarian tissues.** (A–C) Tissue clearing by digestion and expansion. Grids in the background were included to show tissue transparency. Dashed lines in (C): the outline of the planarian body, which is larger than the imaging view. Scale bars: 1 mm. (D,E) Post-expansion images of planarians immunostained for muscle fibers, using either glutaraldehyde (GA) or MA-NHS as linker molecules. Using GA, expansion disrupts muscle fibers, whereas no distortion was observed in MA-NHS linked tissues. Scale bars: 20 μm.

633

**S4 Figure: μExM of *Salmonella enterica* cells *in vitro*.** (A) Representative maximum intensity projection of mCherry-*Salmonella* cells before expansion. (B) After 1 h lysozyme treatment to digest the cell wall, *Salmonella* cells expanded ~2-fold. Note that mCherry (left) and DAPI (right) signals co-localized. (C) Quantification of the expansion of cells in images similar to (B). (D,E) Cells treated while alive with 0.5 mg mL$^{-1}$ lysozyme for 1 h at 37 °C prior to fixation (D), or cultured in an acidic, magnesium-depleted minimal medium (MgM-MES, pH 5.0, used to simulate the low pH, low Mg$^{2+}$ environment of the phagosome) (E) did not expand, suggesting that the cell wall remained intact under these conditions. Scale bars: 10 μm.